

Anisotropy of tracer dispersion in rough model fractures with sheared walls.

Boschan A.^{a,b}, Auradou H.^a, Ippolito I.^b, Chertcoff R.^b, Hulin J.P.^a

^aUniv Pierre et Marie Curie-Paris6, Univ Paris-Sud, CNRS, F-91405. Lab FAST, Bat 502, Campus Univ, Orsay, F-91405, France.

^bGrupo de Medios Porosos, Departamento de Física, Facultad de Ingeniería, Universidad de Buenos Aires, Paseo Colón 850, 1063 Buenos-Aires, Argentina.

Abstract

Dispersion experiments are compared for two transparent model fractures with identical complementary rough walls but with a relative shear displacement $\vec{\delta}$ parallel ($\vec{\delta} \parallel \vec{U}$) or perpendicular ($\vec{\delta} \perp \vec{U}$) to the flow velocity \vec{U} . The structure of the mixing front is characterized by mapping the local normalized local transit time $\bar{t}(x, y)$ and dispersivity $\alpha(x, y)$. For $\vec{\delta} \perp \vec{U}$, displacement fronts display large fingers: their geometry and the distribution of $\bar{t}(x, y)U/x$ are well reproduced by assuming parallel channels of hydraulic conductance deduced from the aperture field. For $\vec{\delta} \parallel \vec{U}$, the front is flatter and $\alpha(x, y)$ displays a narrow distribution and a Taylor-like variation with Pe .

Channelization is a key characteristic of flow and transport in fractured rocks ([12]) and results frequently from the occurrence of relative shear displacements of the two fracture surfaces during fracturation ([14, 8]). Such displacements (named $\vec{\delta}$ thereafter) have been shown both experimentally and numerically ([11, 1]) to create channels and ridges perpendicular to $\vec{\delta}$. Their length depends on the multiscale geometry of the fracture walls and, even for small amplitudes δ , may be a significant fraction of the fracture size. The permeability is then anisotropic: both its value and the correlation length of the velocity field are higher for a mean flow parallel to these channels (*i.e.* perpendicular to $\vec{\delta}$).

The objective of this communication is to demonstrate experimentally that this type of channelization also induces a strong anisotropy of the magnitude and properties of tracer dispersion. This is achieved by comparing dispersion for mean flows parallel and perpendicular to the direction of the channels, but with identical flow parameters and geometry otherwise. A previous work ([4]) studied dispersion in one similar model (with a lower value of δ) but with the different objective of analyzing the influence of the fluid rheology. Here, the dynamics of the process, *i.e.* the variation with distance of the geometry and thickness of the mixing front is more specifically compared in the parallel and perpendicular configurations.

Many experiments on solute spreading in fractures have been reported: [13, 9, 10] observed dispersion coefficients D increasing linearly with the mean flow velocity U (*i.e.* the dispersivity $\alpha = D/U$ is constant).

Preprint submitted to Elsevier

However, these measurements were all realized at the outlet of the sample with no information on the development of the mixing front with distance. Measurements by [15] used radioactive tracers, still with a resolution too low to investigate local spreading. In all these papers, the anisotropy of dispersion is not investigated and (except for [10]) little information is available on the relative position of the fracture walls.

We use transparent model fractures allowing for high resolution optical concentration measurements over their full area. The models are mounted vertically between a light panel and a 16 bits Roper digital camera. Fluid flow takes place between two self-affine rectangular rough walls of same characteristic exponent $H = 0.8$ as in many fractured rocks ([16]). The mean flow velocity \vec{U} is parallel to the length $L_x = 350$ mm of the walls (their width is $L_y = 90$ mm). The two walls are complementary and identical in the two models and they match perfectly when put in contact; then, they are pulled away normal to their mean surface and a lateral shear $\vec{\delta}$, parallel or perpendicular to \vec{U} (*i.e.* to x) is introduced. In these two configurations, referred to as $\vec{\delta} \parallel \vec{U}$ and $\vec{\delta} \perp \vec{U}$, the mean velocity \vec{U} is therefore respectively perpendicular and parallel to the channels created by the shear. Both δ and the mean aperture a are equal to 0.75 mm. The standard deviation of the aperture $\sigma_a = 0.144$ mm is larger than for the similar models of [4] ($\sigma_a = 0.11$ mm): as a result, the flow field is found to be more strongly channelized.

The fluids are shear thinning 1000 ppm solutions of scleroglucan in water with a high constant viscos-

October 30, 2018

ity ($\mu_0 \approx 4500 \text{ mPa}\cdot\text{s}$) at low shear rates $\dot{\gamma} \leq \dot{\gamma}_0$ preventing the appearance of unwanted buoyancy driven flows ([17]). One has $\dot{\gamma}_0 = 0.026 \text{ s}^{-1}$: for a viscous Newtonian flow between parallel plates at a distance a , the corresponding mean velocity is $U_0 = a\dot{\gamma}_0/6 = 3 \times 10^{-3} \text{ mm/s}$. At shear rates $\dot{\gamma} \geq \dot{\gamma}_0$, the viscosity decreases as $\mu \propto \dot{\gamma}^{n-1}$ with $n = 0.26$ (see [4]). One of the fluids contains 0.2 g/l of blue dye and the densities are matched by adding NaCl to the other. The flow velocity U is constant during each experiment with: $0.0024 \leq U \leq 0.24 \text{ mm/s}$ and tracer transport is characterized by the dimensionless Péclet number $Pe = Ua/D_m$ where $D_m = 6.5 \cdot 10^{-10} \text{ m}^2/\text{s}$ is the molecular diffusion coefficient of the dye. The experimental procedure and the determination of dye concentration maps from images recorded at constant time intervals are described by [4].

Fig. 1 shows maps obtained in the two model fractures at two different velocities U . If $\vec{\delta} \perp \vec{U}$, two fingers soar upwards with a large trough in between (Figs. 1b and 1d): they correspond to faster paths parallel to \vec{U} (Fig. 1b) and their amplitude increases with U . For $\vec{\delta} \parallel \vec{U}$, the front is smoother (Figs. 1a and 1c) while its mean slope and the size of the indentations still increase with the velocity.

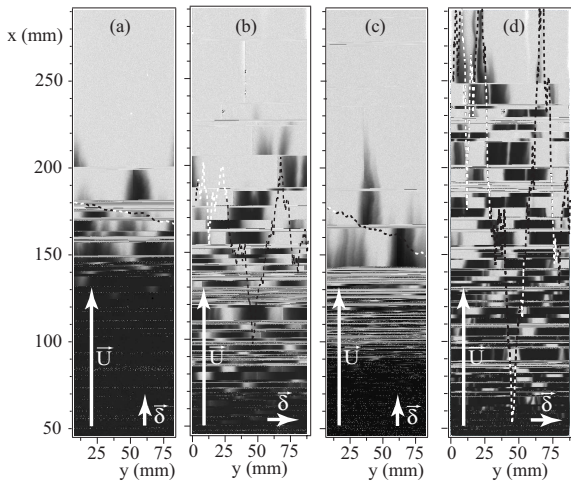


Figure 1: Maps of the relative concentration c of the displaced fluid (white $c = 1$, black $c = 0$) in two transparent models. (a)-(c): $\vec{\delta} \parallel \vec{U}$; (b)-(d): $\vec{\delta} \perp \vec{U}$. Mean velocities: (a)-(b): $U = 0.0125 \text{ mm/s}$, $Pe = 14$; (c)-(d): $U = 0.25 \text{ mm/s}$, $Pe = 285$. The injected volume of displacing fluid is half the void space.

The large structures in Figs. 1b and 1d reflect ve-

locity contrasts between the channels created by the shear. They are well reproduced by modelling the fracture aperture field as a set of independent parallel channels of aperture $a(y) = \langle a(x, y) \rangle_x$ ([1, 2]). A particle starting at a transverse distance y at the inlet is assumed to move at a velocity proportional to $a(y)^{(n+1)/n}$ where $n = 0.26$ for $U > U_0$ and $n = 1$ for $U < U_0$.

The profile $x_f(y, t)$ of the front at a time t is then:

$$x_f(y, t) = \frac{\overline{x(t)} a(y)^{(n+1)/n}}{\langle a(y)^{(n+1)/n} \rangle_y}, \quad (1)$$

where $\overline{x(t)} = \langle x_f(y, t) \rangle_y$ and $\langle a(y)^{(n+1)/n} \rangle_y$ are averages calculated over y . The profiles computed using Eq. (1) and the actual aperture fields appear in Figs. 1a-d as dotted lines (from the above discussion, one assumes that $n = 1$ at the lowest velocity (Figs. 1a and 1b) and $n = 0.26$ at the highest one (Figs. 1c and 1d)). Eq. (1) predicts well the location and shape of the “fingers” and “troughs” at both velocities for $\vec{\delta} \perp \vec{U}$ although their amplitude is slightly underestimated in Fig. 1b. In this latter case, one has $U \sim U_0$, corresponding to a transition regime between the power law and Newtonian rheologies.

These results demonstrate that, for $\vec{\delta} \perp \vec{U}$ (*i.e.* if \vec{U} is parallel to the channels created by the shear), the large scale features of solute transport are determined by the contrasts between the velocities in these channels which increase with their aperture. Then, front spreading is purely convective and the total width Δx of the front parallel to \vec{U} (*i.e.* the distance between the tips of the fingers and the bottom of the troughs) increases linearly with distance as $x \Delta U/U$ ($\Delta U/U =$ typical relative velocity contrast between the different channels). These curves also demonstrate that the difference between the sizes of the fingers in the two cases are accounted for by the different rheological behavior of the fluids: the velocity contrasts (and therefore the size) are amplified for $Pe = 285$ (shear-thinning power law domain) compared to the vicinity of the Newtonian constant viscosity regime ($Pe = 14$).

For $\vec{\delta} \parallel \vec{U}$, the features of the front are also visible at the same transverse distances y in Figs. 1a and 1c: they reflect again a convective spreading of the front due to velocity contrasts between the flow paths. However, in contrast with the previous case $\vec{\delta} \perp \vec{U}$, these features (except for the small global slope of the front) are not reproduced by the theoretical model (dotted line): this was to be expected since its underlying hypothesis are not satisfied for $\vec{\delta} \parallel \vec{U}$. The time variations of the local concentration $c(x, y, t)$ on individual pixels complement the above study by providing quantitative informa-

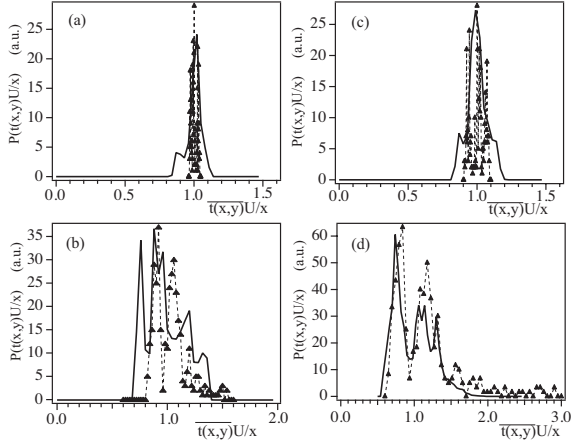


Figure 2: Histograms of the experimental normalized local transit time $\overline{t(x,y)U/x}$ (continuous lines) for the same models and Pe values as in Figs. 1 (the letters corresponding to the different experiments are the same in both graphs). The distribution of $\overline{t(x,y)U/x}$ has been computed in the upper fifth of the length of the model to make meaningful comparisons with the distribution of the theoretical transit times (\blacktriangle symbols and dotted lines) determined from Eq. (1).

tion on the interplay of convective and diffusive mechanisms. For all the experiments, $c(x, y, t)$ is found to be well fitted by solutions of a classical 1D convection-dispersion equation for a step-like initial variation of c at the inlet ($x = 0$):

$$c(x, y, t) = \frac{1}{2} \left(1 + \operatorname{erf} \frac{t - \overline{t(x,y)}}{\sqrt{4D(x,y)t}} \right), \quad (2)$$

Here, $\overline{t(x,y)}$ and $D(x,y)$ are the mean transit time and apparent dispersion coefficient deduced from the time variation of the relative concentration $c(x, y, t)$ of the displaced fluid at point (x, y) (transverse dispersion is neglected here). It will be shown below that the two parameters provide complementary information: $D(x, y)$ (or rather the dispersivity $\alpha(x, y) = D(x, y)/U$) characterizes the local thickness of the mixing front while $\overline{t(x,y)}$ is related to its global geometry.

For each experiment, $\overline{t(x,y)}$ and $D(x,y)$ are determined for all pixels inside the field of view. Fig. 2 compares experimental and theoretical probability distributions of the normalized times $\overline{t(x,y)U/x}$ for the same experiments as Fig. 1. The theoretical distribution is obtained by taking $\overline{t(x,y)U/x} = x_f(y, t)/x(t)$, computing the ratio $x_f(y, t)/x(t)$ by means of Eq. (1) for all y

values and determining finally the distribution of the results. As expected, the distributions are much broader for $\vec{\delta} \perp \vec{U}$ (Figs. 2b-d) than for $\vec{\delta} \parallel \vec{U}$ (Figs. 2a-c). For $Pe = 285$, the experimental distribution for flow parallel to the channels coincides very well with the theoretical one and displays two peaks reflecting the structuration of the flow. At $Pe = 14$, the width and global shape of the experimental and theoretical distributions are overall similar and narrower than for $Pe = 285$ due to the lower velocity contrast in the Newtonian limit. For $\vec{\delta} \parallel \vec{U}$ (Figs. 2a-c), the distribution at both Péclet numbers is much narrower than for $\vec{\delta} \perp \vec{U}$. The mean peak corresponds to $\overline{t(x,y)U/x} \approx 1$; its width increases with Pe (again likely due to an increase of the velocity contrasts) and is similar to that of the theoretical distributions. The experimental distribution displays however additional “aisles”: these reflect likely complex paths deviating from straight trajectories parallel to \vec{U} .

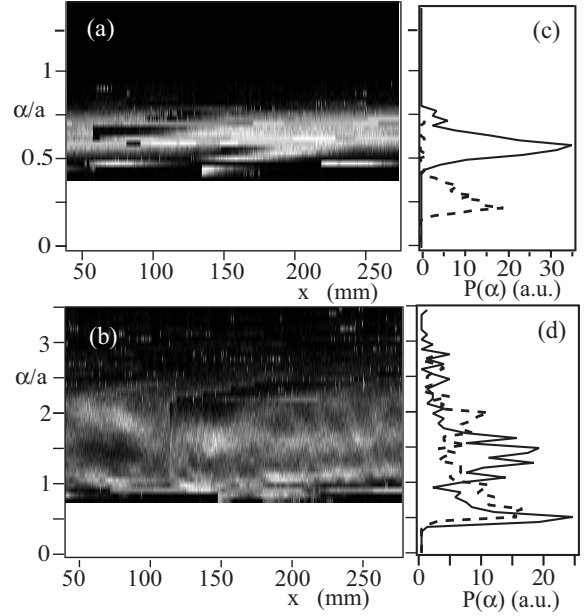


Figure 3: (a)-(b): Histograms (grey levels) of the values of the normalized local dispersivity $\alpha(x, y)/a$ (vertical scale) as a function of the distance x (horizontal scale) for $Pe = 285$. White: maximum probability, black : zero probability. (c), (d): Histograms obtained at $x = 240$ mm for $Pe = 285$ (continuous line) and $Pe = 14$ (dashed line). (a), (c): $\vec{\delta} \parallel \vec{U}$; (b), (d): $\vec{\delta} \perp \vec{U}$.

While, from the above results, the overall geometry of the mixing front seems to be determined mainly by

convective effects, we examine now the relative influence of convection and diffusion on the local width of this front: this may be characterized by the variation of the local dispersivity $\alpha(x, y)$ with Pe . Figs. 3a-b display, for each value of x (horizontal scale), the histogram (coded in grey levels) of the corresponding values of $\alpha(x, y)/a$ (vertical scale).

For $\vec{\delta} \parallel \vec{U}$, the probability distribution of $\alpha(x, y)/a$ is narrow, particularly at high flow velocities (Figs. 3a and c). Moreover, the mean value varies little with the distance x and reaches a constant value $\alpha(Pe)/a$ for $x \geq 100\text{mm}$ (see inset of Fig. 4). The increase with time of the local front thickness is therefore diffusive and can be characterized by a single dispersivity value $\alpha(Pe)/a$.

For $\vec{\delta} \perp \vec{U}$ (Figs. 3b and d), the distribution of the values of α/a is much broader and displays a “tail” at large values of α/a . At the two highest velocities, the distribution displays two peaks (solid curve in Fig. 3). While the value of $\alpha(x)/a$ corresponding to the peak(s) seems to reach a limit at long distances x , the global width of the distribution keeps increasing with x . In contrast to the case $\vec{\delta} \parallel \vec{U}$, the increase of the local thickness of the mixing front with x is not simply diffusive and cannot be characterized by a single dispersivity parameter.

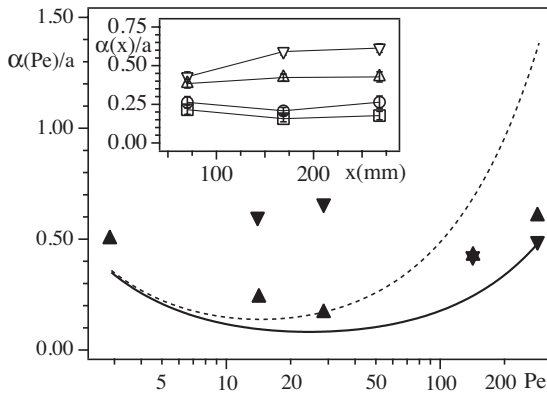


Figure 4: Variation of the normalized dispersivity α/a as a function of Pe . (\blacktriangle) $\vec{\delta} \parallel \vec{U}$: mean value of α/a . (\blacktriangledown) $\vec{\delta} \perp \vec{U}$: value corresponding to the first peak in the distribution of α/a . Continuous and dashed lines: Taylor dispersion between parallel plates respectively for a power law fluid of exponent $n = 0.26$ and a Newtonian fluid ($n = 1$). Inset: variation of the mean value $\langle \alpha(x, y) \rangle_x$ as a function of the distance x for $\vec{\delta} \parallel \vec{U}$; $Pe = 285$ (∇), $Pe = 142$ (\triangle), $Pe = 28.5$ (\square), $Pe = 14$ (\circ).

The variation of $\alpha(Pe)$ with Pe for $\vec{\delta} \parallel \vec{U}$ displayed in Fig. 4 provides quantitative information on the lo-

cal dispersion mechanisms: the values are similar (although slightly higher) to the predictions for Taylor dispersion with a power law fluid (continuous line). At low Pe 's, the values obtained for $n = 1$ (dashed line) and for $n = 0.26$ are similar and the transition towards a Newtonian behaviour should not influence the variations. A dominant contribution of Taylor dispersion has already been demonstrated in models with a randomly distributed aperture of short correlation length ([7]); however, at low Pe 's, an additional geometrical dispersion regime ($\alpha = cst(Pe)$) was observed and is not present here.

In the opposite case ($\vec{\delta} \perp \vec{U}$), no single value of α characterizes dispersion in the whole model. However, the first peak in the distribution of α likely reflects dispersion in regions of low transverse gradient of the mean front velocity in the plane of the model: there, additional spreading due to transverse diffusion in the velocity gradient should be reduced. The values of α/a corresponding to this first peak have therefore been plotted in Fig 4 (\blacktriangledown) as a function of Pe . At high velocities, they are indeed close to those corresponding to Taylor dispersion (and to the other model); at low velocities, they remain higher.

Overall, the present experiments demonstrate that solute dispersion in a channelized rough fracture depends crucially of the orientation of the flow. Optical measurements allowed us to characterize the dynamics of dispersion at both the global and local scales from mean transit times and local dispersivities deduced from local concentration variations.

For $\vec{\delta} \perp \vec{U}$ (\vec{U} parallel to the channelization), the large scale geometry of the displacement front is controlled by the velocity contrasts between the channels. At all Pe values ($14 \leq Pe \leq 285$) the geometries of the large fingers and troughs in the front and the distribution of the local transit times $\overline{t(x, y)U}/x$ are well predicted from a transverse effective permeability profile computed using the aperture field. Moreover, differences between the finger sizes at low and high Pe 's are explained by variations of the fluid rheology (shear-thinning at high Pe 's and Newtonian at low ones). These results confirm fully the convective origin of the large scale structures of the front and the relevance of local measurements all along the flow paths: measuring only variations of the mean concentration at the outlet (as is often done practically) and fitting it to a solution of a convection-diffusion equation might indeed lead to an incorrect identification of such processes as geometrical dispersion.

For $\vec{\delta} \parallel \vec{U}$ (\vec{U} perpendicular to the channelization), the front is flatter and the distribution of the transit times

is narrower than for $\vec{\delta} \perp \vec{U}$; this reflects a more effective sampling of the velocity heterogeneities by the solute particles. As could be expected, the remaining geometrical features of the front cannot be predicted by the channel model: however they are still observed at the same transverse locations at all velocities and remain of similar amplitudes (taking into account the variations of the rheology). This suggests that these features are again of convective origin.

Still for $\vec{\delta} \parallel \vec{U}$, the variation of the local front thickness is diffusive and well characterized by a single mean dispersivity $\alpha(Pe)$; its dependence on Pe suggests a dominant influence of Taylor dispersion. For $\vec{\delta} \perp \vec{U}$, in contrast, the broad distribution of $\alpha(x, y)$ does not allow one to define a meaningful global dispersivity. In addition, even the lowest values of $\alpha(x, y)$ (corresponding to simple flow paths) are larger than those expected for Taylor dispersion except at the highest Pe values; values corresponding to Taylor dispersion are also expected at smaller values of δ leading to a reduced disorder of the flow field [4]. This latter difference, as well as the tail in the distribution, reflect the increasing influence of transverse molecular diffusion inducing tracer exchange with adjacent flow paths of different velocities and enhancing dispersion.

This set of results is highly relevant to the interpretation of field observations ([3]). However, the influence of the length of the samples is an important issue and will need to be investigated before transposing these results. In particular, although the front geometries are determined in both configurations by spatial variations of the flow velocities, a geometrical dispersion regime has never been observed, in contrast with experiments on rough fractures with a small correlation length of the aperture ([7]). For much longer fractures, transverse diffusion might be large enough for solute particles to sample the whole distribution of local velocities and reach such a global diffusive spreading regime. In the case of a broad distribution of the hydraulic conductivities, one might also observe instead an anomalous dispersion regime as suggested by [5] and [6]. Because of the specific correlations of the flow velocity field for self-affine wall geometries ([1]), the corresponding exponent would then likely depend on the characteristic roughness exponent of the fracture walls.

1. Acknowledgments

We are indebted to R. Pidoux for his assistance. HA and JPH are supported by CNRS through the GdR No. 2990) and by the EHDRA (European Hot Dry Rock Association). This work was greatly facilitated by a

CNRS-Conicet Collaborative Research Grant and by the Ecos Sud A03E02 program.

References

- [1] Auradou, H., G. Drazer, A. Boschan, J. P. Hulin, and J. Koplik (2006), Shear displacement induced channelization in a single fracture, *Geothermics*, 35, 576–588.
- [2] Auradou, H., A. Boschan, R. Chertcoff, S. Gabbanelli, J.P. Hulin and I. Ippolito(2008), Enhancement of velocity contrasts by shear-thinning solutions flowing in a rough fracture, *J. Non-Newtonian Fluid Mech.*, 153, 53–61.
- [3] Becker, M. and A. Shapiro (2000), Tracer transport in fractured crystalline rock: Evidence of nondiffusive breakthrough tailing, *Water Resour. Res.*, 36, 1677–1686.
- [4] Boschan A., H. Auradou, I. Ippolito, R. Chertcoff and J.P. Hulin (2007), Miscible displacement fronts of shear thinning fluids inside rough fractures. *Water Resour. Res.*, 43, W03438.
- [5] Bouchaud J.P., A. Georges and P. Le Doussal (1987), Diffusion anormale dans les milieux désordonnés : piégeage, corrélations et théorèmes de la limite centrale, *J. Phys. France* 48, 1855–1860.
- [6] Dentz M., Le Borgne T. and Carrera J. (2008) Effective transport in random shear flows *Phys. Rev. R* 77, 020101.
- [7] Detwiler R., H. Rajaram, and R. J. Glass (2000), Solute transport in variable aperture fractures: An investigation of the relative importance of Taylor dispersion and macrodispersion, *Water Resour. Res.*, 36, 1611–1625.
- [8] Gentier, S., E. Lamontagne, G. Archambault, and J. Riss (1997), Anisotropy of flow in a fracture undergoing shear and its relationship to the direction of shearing and injection pressure, *Int. J. Rock Mech. & Min. Sci.*, 34(3-4), 412.
- [9] Keller A.A., Roberts P.V., Blunt M.J. (2000) Effect of fracture aperture variations on the dispersion of contaminants, *Water Resour. Res.*, 35, 55–63.
- [10] Lee J., J.M. Kang and J. Choe (2003) Experimental analysis on the effects of variable apertures on tracer transport, *Water Resour. Res.*, 39 (1), 1015, doi:10.1029/2001WR001246, 2003.
- [11] Matsuki K., Y Chida, K. Sakaguchi and P.W.J. Glover (2006), Size effect on aperture and permeability of a fracture as estimated in large synthetic fractures, *Int. J. Rock Mech. Min. Sci.*, 43, 726–755.
- [12] Committee on Fracture Characterization and Fluid Flow, National Research Council (1996), *Rock Fractures and Fluid Flow: Contemporary Understanding and Applications*, National Academy Press, Washington, D.C.
- [13] Neretnieks, I., T. Eriksen, and P. Tahtinen (1982), Tracer movement in a single fissure in granite rock: Some experimental results and their interpretation, *Water Resour. Res.*, 18, 849–858.
- [14] Olsson, W. A., and S. R. Brown (1993), Hydromechanical response of a fracture undergoing compression and shear, *Int. J. Rock Mech. Min. Sci. & Geomech. Abs.*, 30(7), 845–851.
- [15] Park C.K., T.T. Vandergraaf, D.J. Drew and P.S. Hahn (1997), Analysis of the migration of nonsorbing tracers in a natural fracture in granite using a variable aperture fracture model, *J. Cont. Hydro.* 26, 97–108.
- [16] Poon C., R. Sayles, T. Jones, Surface measurement and fractal characterization of naturally fractured rocks, *J. Phys. D: Appl. Phys.*, 25 (1992) 1269–1275.
- [17] Tenchine S. and Ph. Gouze (2005) Density contrast effects on tracer dispersion in variable aperture fractures, *Advances in Water Resources*, 28, 273–289.